Molecular-Scale Functionality on Graphene To Unlock the Energy Capabilities of Metal Hydrides for High-Capacity Lithium-Ion Batteries

Guanglin Xia,[†,‡,#] Baoping Zhang,[†,#] Xiaowei Chen,[§] Dalin Sun,[†] Zaiping Guo,[‡] Fuxin Liang,[∥] Weidong Zou,[§] Zhenzhong Yang,*[,∥] and Xuebin Yu*[,†]

[†]Department of Materials Science, Fudan University, Shanghai 200433, China
[‡]Institute for Superconducting and Electronic Materials, University of Wollongong, North Wollongong, New South Wales 2522, Australia
[∥]State Key Laboratory of Polymer Physics and Chemistry, Institute of Chemistry, Chinese Academy of Sciences, Beijing 100190, China
[§]Department of Physics, Jimei University, Xiamen 361021, China

Ⓢ Supporting Information

ABSTRACT: Metal hydrides have attracted great intentions as anodes for lithium-ion batteries (LIBs) due to their extraordinary theoretical capacity. It is an unsolved challenge, however, to achieve high capacity with stable cyclability, owing to their insulating property and large volume expansion upon lithium storage. Here, we introduce self-initiated polymerization to realize molecular-scale functionality of metal hydrides with conductive polymer, that is, polythiophene (PTh), on graphene, leading to the formation of MgH_2@PTh core−shell nanoparticles on graphene. The nanoscale characteristics of MgH_2 not only relieve the induced stress upon volume changes but also allow fast diffusivity and high reactivity for Li-ion transport. More importantly, the conformal coating of ultrathin PTh membrane can effectively suppress the detrimental reactions between MgH_2 and electrolyte, provide enhanced performance with facile electron and Li^+ transport, and preserve its structural integrity, attributed to the strong molecular interaction between PTh and MgH_2 as well as its various products during electrochemical reactions. With this structure, a high reversible specific capacity of 1311 mAh g^{-1} at 100 mA g^{-1}, excellent rate performance of 1025 mAh g^{-1} at 2000 mA g^{-1}, and a capacity retention of 84.5% at 2000 mA g^{-1} after 500 cycles are observed for MgH_2@PTh nanoparticles as anode for LIBs.

KEYWORDS: lithium-ion batteries, metal hydride, magnesium hydride, graphene, self-assembly
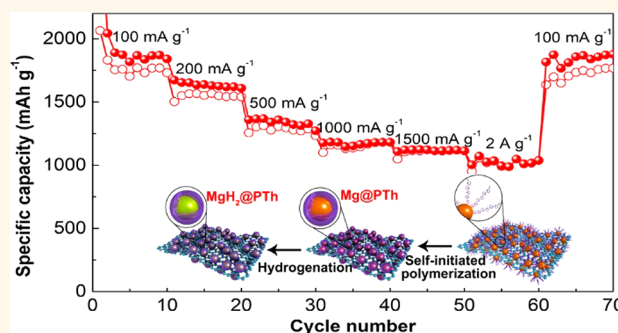
R echargeable lithium-ion batteries (LIBs) are one of the predominant power sources for applications in the portable electronics market and are believed to be promising candidates for electrical vehicle and grid-scale energy storage due to their high energy density, high voltage, and environmental friendliness.[1−5] The most common commercial graphite anode materials, however, exhibit a relatively low theoretical specific capacity of 372 mAh g^{-1}. In order to meet the ever-growing energy and power demands of electrical devices, considerable research efforts have been devoted to the development of advanced electrode materials with high energy density, power density, and long cycle life at

low cost.[6−8] Accordingly, the use of metal hydrides has been proposed by Oumellal *et al.* in 2008 and further developed as very high capacity materials for LIBs.[9,10] It has been experimentally demonstrated that several metal hydrides could react with lithium during the past decade based on the following reaction: $MH_x + xLi^+ + xe^- \rightleftharpoons M + xLiH$.[9,10] Among them, magnesium hydride (MgH_2) in particular is attracting extensive attention in view of its high theoretical capacity of

2038 mAh g^{-1}, owing to the much lower molecular weights of magnesium and hydrogen, and the safe potential window of 0.1−0.5 V vs Li$^+$/Li^0 with the low cost and high natural abundance (∼2.5% of earth's surface composition, and virtually in unlimited amounts in seawater).[9] It has been found that a full discharge capacity of MgH$_2$ could be achieved in the first cycle and a high reversible capacity of 1480 mAh g^{-1} is obtained in liquid electrolyte at room temperature, which is 4 times that of traditional Li/graphite electrodes at a suitable potential (0.5 V vs Li$^+$/Li^0) for a negative electrode.[9] Additionally, MgH$_2$ as anode material displays the lowest value of polarization (0.2 V vs Li$^+$/Li^0) ever reported compared to all other conversion electrodes due to the facile transportation of hydrogen, which could effectively reduce the self-heating effect during cycling and the risk of thermal runaway.[9−11] Unfortunately, the practical application of MgH$_2$ as anode is significantly hindered by the rapid capacity fading during cycling (a capacity of <200 mA h g^{-1} after only 10 complete cycles), poor rate capability, and low Coulombic efficiency, which is attributed to its intrinsically low electronic conductivity, aggregation, and loss of electrical contact with the current collector induced by large volume changes and pulverization occurring during the lithiation−delithiation cycling.[12,13]

In the case of the electrode materials that experience large volume changes during charge/discharge in liquid electrolyte at room temperature, effective mitigation of the negative impact of the enormous volumetric changes on the electrochemical performance is the key challenge to enable the practical application of this class of alloying or conversion reaction electrode materials.[14] Recently, extensive research on conversion reaction electrodes has demonstrated that decreasing particle size or electrode nanostructuring is a common strategy to enhance their rate capability by effectively shortening the Li$^+$ diffusion distance and enabling the electrode to withstand high volumetric strains associated with repeated lithium insertion/extraction.[15] Building core−shell nanostructures by integrating electroactive materials with conducting additives, such as carbon or conductive polymer, as the shells has also been reported to improve their electrical conductivity and prevent agglomeration, leading to enhanced electrochemical performance of the active materials.[16−23] For example, Wu and co-workers reported the formation of CuO@carbon-nitride core−shell nanocable array, which could benefit the reversible accommodation of the volume change of the CuO active materials, leading to a reversible capacity as high as 669 mAh g^{-1} after 200 cycles.[14] The core−shell assembly of graphene around Fe$_2$O$_3$ could achieve a high reversible capacity, significantly enhanced cycling stability, and excellent rate capacity of Fe$_2$O$_3$ compared with pristine Fe$_2$O$_3$, which is mainly attributed to the important role of graphene shell in preventing aggregation, buffering the volume change, maintaining the integrity of the active materials, and improving the conductivity of the electrode.[24] In addition, Zhu and co-workers reported that building the Fe$_3$O$_4$@polypyrrole core−shell structures could effectively facilitate the rapid ion/electron transportation for electrochemical reaction, leading to superior lithium storage performance.[25] More recently, uniform distribution of Sn in the core−shell TiO$_2$−Sn@carbon nanofibers has been demonstrated as an effective strategy to not only buffer the volume variation of Sn and prevent the aggregation and pulverization during cycling discharge/charge process but also improve the electronic conductivity of the

electrode.[26] Unfortunately, although a significant improvement has been demonstrated for those metal-oxide (nitride and/or sulfide)-based anode materials, based on combining the advantages of these two strategies, the synthesis of anodes with stable nanostructures is still challenging due to the lack of rational design on the molecular level. In particular, the practical performance of MgH$_2$ anode material has fallen far short of the theoretical promise, and the related development has been rather slow because of the limited application of existing anode technologies in this field. A recent study in our group has demonstrated that anchoring MgH$_2$ nanoparticles (NPs) on graphene, combined with poly(methyl methacrylate) (PMMA) as the binder, could effectively improve the reversibility of MgH$_2$-based anodes.[27] Only a reversible capacity of 395 mAh g^{-1}, however, could be maintained at 2000 mA g^{-1} after 1000 cycles. Therefore, in order to satisfy the continuing demand for advanced LIBs with higher capacity, the energy capacity of MgH$_2$-based anodes needs to be urgently unlocked to develop high-performance LIBs via the uniform and rational integration of both nanostructure engineering and hybridization based on molecular level.

In this study, to achieve a high reversible capacity with stable cyclability, we have fabricated an anode consisting of graphene-supported MgH$_2$@polythiophene (PTh) core−shell NPs (G/MgH$_2$@PTh), using a self-initiated polymerization induced by Mg nanocrystals (NCs) to unlock the energy capabilities of metal hydrides. First, graphene, a monolayer of carbon atoms arranged in a honeycomb network, exhibits many amazing properties, such as high electrical conductivity, high surface area, and excellent chemical stability, which makes it a good carbon platform to improve the electrochemical properties of MgH$_2$ anodes.[28,29] Taking advantage of the Mg-induced selective and self-limiting polymerization of thiophene and the favorable molecular adsorption of thiophene on Mg NCs, MgH$_2$@PTh core−shell NPs uniformly distributed on graphene are built after the complete hydrogenation of Mg NCs, leading to molecular-scale control of the functionality of electroactive MgH$_2$ NCs with a self-induced electronically conductive PTh coating. This designed structure is ideal for homogeneous coating of MgH$_2$ NCs and inhibiting the aggregation of MgH$_2$ NCs, leading to long-term stable cycling performance with high capacity. Furthermore, the intimate and homogeneous contact between MgH$_2$ NCs and electron-conducting PTh nanofilms, as well as cross-linked graphene, offers fast transport pathways for electrons and Li$^+$ diffusion, effectively absorbing the mechanical stress induced by volume expansion and efficiently preventing the detrimental reactions between MgH$_2$ and electrolyte. Consequently, a LIB anode with this purposely optimized nanostructure was able to deliver the high reversible capacity of 1311 mAh g^{-1}, based on the mass of MgH$_2$ at 100 mA g^{-1}, and a significantly enhanced reversible capacity of 884 mAh g^{-1} at a high current density of 2000 mA g^{-1} after 500 cycles.

RESULTS AND DISCUSSION

Figure 1a illustrates the detailed synthesis procedure for G/MgH$_2$@PTh. First, MgH$_2$ NCs homogeneously distributed on graphene (G/MgH$_2$ NCs) were facilely synthesized according to the hydrogenation-induced self-assembly of dibutyl magnesium on graphene, and they were then transformed into graphene-supported Mg NCs via simple thermal annealing as the functional nanoreactor.[30] Subsequently, a Mg-induced reductive transformation based on the following reaction: nMg
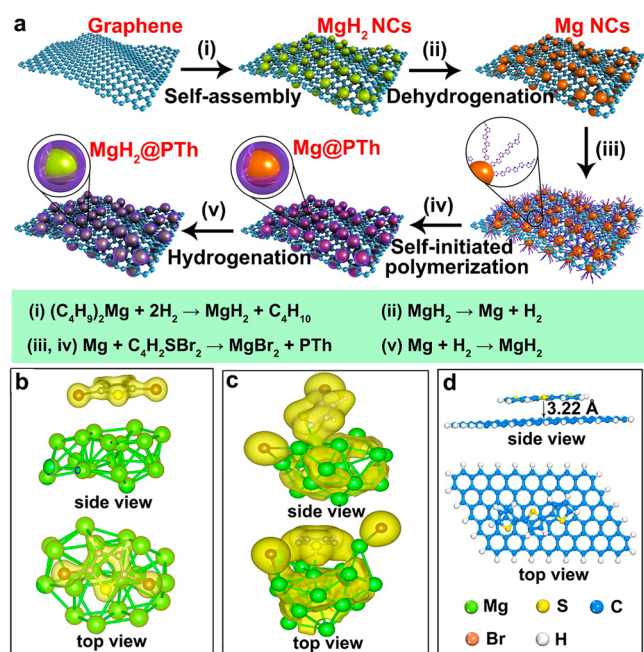
Figure 1. (a) Schematic illustration of the formation of G/MgH$_2$@PTh. Structures of the most stable binding configurations from DFT calculations after full relaxation of C$_4$H$_2$SBr$_2$ on pure Mg$_{18}$ clusters (b) and C$_4$H$_2$SMgBr on pure Mg$_{17}$ clusters (c). Charge density isosurfaces are shown. (d) Atomic structures (top and side views) for the adsorption of PTh on graphene in the most stable configuration.

$+ n$C$_4$H$_2$SBr$_2$ → nMgBr$_2$ + PTh resulted in a homogeneous and selective coating of PTh on the Mg NCs to form Mg@PTh core−shell NPs distributed on graphene (G/Mg@PTh).[31] Furthermore, in order to investigate the molecular interactions during the self-initiated polymerization, density functional theory (DFT) calculations were conducted. It was calculated that, under the most stable geometrical configurations, the binding energy between C$_4$H$_2$SBr$_2$ and Mg was 0.55 eV (Figure 1b), indicating the favorable adsorption of the thiophene monomer on the surface of Mg NCs in the initial stage of polymerization. A stronger molecular interaction between C$_4$H$_2$SMgBr, which is the intermediate product of the reaction, and Mg NCs is observed as evidenced by the increase in binding energy to 2.68 eV, and there is even a large transfer of charge from Mg to C$_4$H$_2$SMgBr due to the low electronegativity of Mg (Figure 1c). This finding indicates that, by virtue of the favorable molecular interaction between Mg NCs and C$_4$H$_2$SBr$_2$ and/or C$_4$H$_2$SMgBr, the ultrathin PTh membrane synthesized *in situ* could be uniformly coated on the surfaces of the individual Mg NCs. Finally, G/MgH$_2$@PTh was obtained through hydrogenation of the Mg NCs in G/Mg@PTh.

The morphology of the as-synthesized products was subsequently investigated by field-emission scanning electron microscopy (FE-SEM) and transmission electron microscopy (TEM). Figure 2a shows the formation of homogeneous MgH$_2$ NCs with an average particle size of around 13.8 nm uniformly anchored on graphene after the hydrogenation-induced self-assembly process (Figure S1), which offers facile pathways for the uniform adsorption of thiophene monomer and the subsequent homogeneous functionality of MgH$_2$ NCs with
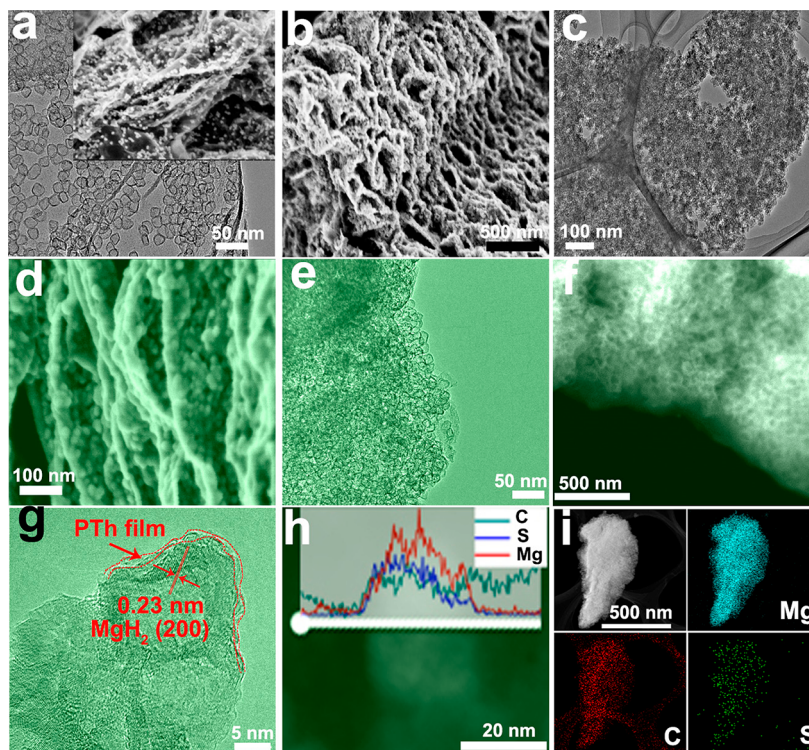

Figure 2. (a) TEM image of G/MgH$_2$ NCs. The inset shows the corresponding SEM image. (b) SEM and (c) TEM images of G/Mg@PTh. (d) SEM, (e) TEM, (f) STEM, and (g) HRTEM images of G/MgH$_2$@PTh. (h) EDS line scan (route marked by white line) of G/MgH$_2$@PTh on an STEM image. The inset shows the corresponding element distributions of carbon, magnesium, and sulfur, respectively. (i) Elemental mapping of G/MgH$_2$@PTh.

PTh films. Meanwhile, the flexible graphene provides stable structural support for the following chemical reaction. X-ray powder diffraction (XRD) measurements demonstrated the formation of cubic MgH_2 (Figure S2), and the X-ray photoelectron spectroscopy (XPS) (Figure S3) results also confirmed the presence of characteristic Mg–H bonds belonging to MgH_2. After the dehydrogenation process *via* thermal treatment at 300 °C, the homogeneous distribution of Mg NCs is well preserved with no visible aggregation (Figure S4), and the formation of Mg NCs could be clearly supported by XRD patterns (Figure S2). It was further adopted as the functional and robust nanoreactor to realize the self-initiated polymerization of thiophene monomer into PTh on the surfaces of the Mg NCs. The completion of the polymerization reaction could be attested by the formation of $MgBr_2$ in the product of the solution after the removal of solvent and G/Mg@PTh (Figure S5), and two typical Raman scattering peaks at 671 and 1455 cm^{-1}, corresponding to the C–S stretching bands and the symmetric stretching vibrations of the aromatic C=C ring bond of PTh, respectively, are present in G/Mg@PTh (Figure S6), which directly demonstrates the successful formation of PTh in the G/Mg@PTh composite.[32] Furthermore, due to the presence of graphene as structural support, the homogeneous distribution of Mg NCs on graphene is well maintained without obvious agglomeration or growth, as confirmed by representative FE-SEM and TEM images of G/Mg@PTh (Figure 2b, c), and the uniform coating of PTh can be clearly observed attributed to both the selective and self-limiting reaction and the favorable adsorption between Mg NCs and the monomer.

After the hydrogenation of the Mg NCs in G/Mg@PTh into MgH_2 NCs, XRD patterns confirm the synthesis of MgH_2 with the complete absence of the precursor Mg NCs (Figure S2), while the characteristic peaks of PTh remain unchanged in the Raman spectrum of G/MgH_2@PTh (Figure S7), validating the complete transformation of MgH_2 from Mg NCs and the good preservation of PTh during the hydrogenation process. More importantly, the G/MgH_2@PTh perfectly maintains the high monodispersivity of the MgH_2 NCs on graphene, with the entire surface uniformly covered by ultrathin PTh membrane, as illustrated in the SEM (Figures 2d), TEM (Figure 2e), and STEM (Figure 2f) images, and this could be further supported by the high-resolution SEM images obtained at different multiple spots (Figure S8). The sandwich-like morphology homogeneously embedded with MgH_2@PTh core–shell NPs ensures good electrical connection between the electroactive particles. A high-resolution TEM (HRTEM) image reveals the uniform core–shell structure of MgH_2@PTh NPs uniformly distributed on a graphene layer (Figure 2g), in which the entire surface of the MgH_2 NCs is uniformly covered with a continuous amorphous layer of PTh. By comparison, only a clear crystal boundary is observed for the MgH_2 NCs in G/MgH_2 NC (Figure S9). In addition, compared to bare G/MgH_2 NC, the signals in the dark-field TEM images (Figure S10) of G/MgH_2@PTh become blurrier due to the covering of MgH_2 NCs with PTh membrane. In order to gain a clear observation of the homogeneous coating of PTh on MgH_2 NCs, G/MgH_2@PTh was soaked in HCl solution to etch away the inner MgH_2 NCs. The TEM images (Figure S11) obviously disclose that the conformal shape of the PTh membrane with an ultrathin thickness of ~2 nm and its amorphous nature is well maintained after strong sonication. As a result, the average particle size of MgH_2 NCs in G/

MgH_2@PTh increases from 13.8 to 15.6 nm after the formation of PTh membrane on the surface of MgH_2 NCs (Figure S1), indicating the homogeneous coating of PTh membrane. The PTh membrane is uniformly distributed on the graphene with only partial hollow NPs depressed into it due to the disappearance of the supporting structure of inner MgH_2 NCs. This also demonstrates the satisfactory resilience of PTh membrane under mechanical forces, which makes it well suited to accommodate the volume expansion of metal hydrides during repeated lithiation/delithiation processes. The intimate interface interaction between PTh, which is an electron-conducting polymer, and MgH_2 in the core–shell nanostructure could further effectively enhance the electrical conductivity from MgH_2 to the current collector and, meanwhile, alleviate the volume changes from lithium extraction/insertion during cycling. Interestingly, it is found that the binding energy between the PTh membrane and the graphene obtained from DFT calculations reaches as high as 1.42 eV (Figure 1d), while the binding energy of the MgH_2-graphene system is only 0.3 eV (Figure S12), suggesting the much more favorable adsorption between PTh and graphene. Therefore, the homogeneous functionality of MgH_2 with PTh membrane could further facilitate the robust anchoring of monodisperse MgH_2 on graphene through the strong molecular interaction between PTh and graphene, thereby preventing aggregation during the lithiation and delithiation over the course of long-term cycling. The porous structure of G/MgH_2@PTh resulting from the assembly of graphene and MgH_2@PTh NPs certified by SEM and TEM images was further investigated by nitrogen sorption isotherms, exhibiting typical type-IV behavior with an obvious hysteresis loop between relative pressures (P/P_0) of 0.5 and 1.0, which is the characteristic of the presence of mesopores (Figure S13a). The Brunauer–Emmett–Teller (BET) surface area of G/MgH_2@PTh is calculated to be as high as 153 m^2 g^{-1}, with a wide pore size distribution from 3 to 20 nm (Figure S13b), validating its mesoporous structure. The abundant porosity with large surface area is beneficial for accelerating the mass diffusion of electrolyte and alleviating the volume changes of MgH_2 anode during cycling charge/discharge processes, leading to improved electrochemical performance. Furthermore, the elemental line-scan profiles on the graphene-supported MgH_2@PTh core–shell NPs show single Gaussian distributions across the particle for the elements C, Mg, and S, confirming that the conductive PTh membrane is uniformly coated on the surfaces of the MgH_2 NCs. The energy dispersive X-ray (EDX) spectrum of G/MgH_2@PTh also demonstrates the presence of the elements C, Mg, and S (Figure S14), and the corresponding elemental mapping (Figure 2i) authenticates the homogeneous distribution of Mg, C, and S in the composite, providing further evidence for the uniform functionality of MgH_2 NCs with PTh membrane. Moreover, the HRTEM image of G/MgH_2@PTh (Figure 2g) displays clear lattice fringes with a *d*-spacing of ~0.23 nm, corresponding to the (200) lattice planes of MgH_2, which is in good agreement with the XRD results.

Further evidence for the formation of MgH_2 NCs in the as-prepared composite is obtained from the Raman spectra of G/MgH_2@PTh and G/MgH_2 NCs (Figure S7), which unveil the characteristic Raman-active E_g phonons of MgH_2 at 952 cm^{-1}.[33] Additionally, two broad peaks at round 1350 and 1593 cm^{-1} are ascribed to the D and G bands of graphene, corresponding to sp^3-type disordered carbon atoms in the
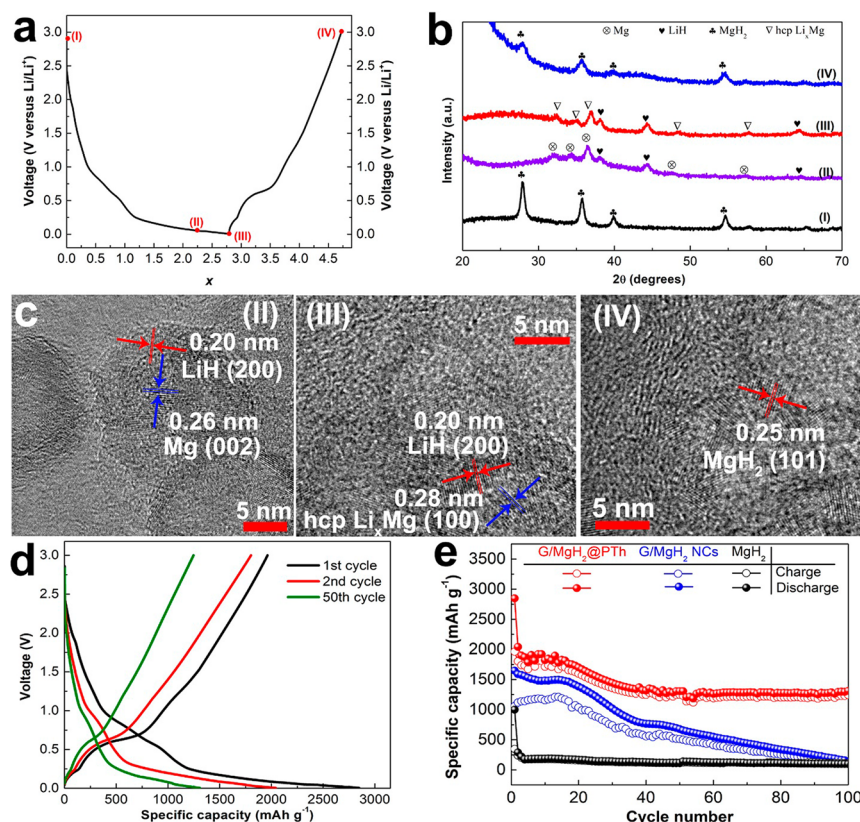
Figure 3. (a) Evolution of the potential (V) as a function of x (x = lithium mole fraction) for the G/MgH$_2$@PTh electrode at 100 mA g^{-1} in the first cycle. (b) *Ex situ* XRD patterns of G/MgH$_2$@PTh electrode collected at the selected charged/discharged states. (c) HRTEM images of G/MgH$_2$@PTh electrode at the selected charged/discharged states. (d) Charge and discharge curves of the G/MgH$_2$@PTh electrode at 100 mA g^{-1} in the first, second, and 50th cycles. (e) Cycling performance of G/MgH$_2$@PTh electrode at 100 mA g^{-1} compared with G/MgH$_2$ NCs and MgH$_2$ particles.

hexagonal graphite network and the in-plane vibrational mode of sp^2-bonded carbon atoms, respectively. The intensity of the D band is higher than that of the G band, which indicates a more disordered stack of graphene in the hybrid, favoring the diffusion of Li ions.[34] In addition, the chemical composition of G/MgH$_2$@PTh was investigated by XPS, which demonstrated the presence of C, Mg, and S in the composite (Figure S15a), validating the high purity of the as-prepared sample. Moreover, the high-resolution Mg 2p spectrum and the S 2p XPS spectrum (Figures S15b, c), composed of S 2p$_{3/2}$ and S 2p$_{1/2}$ peaks attributed to the sulfur in PTh membrane, provide additional evidence for the existence of MgH$_2$ and PTh in G/MgH$_2$@PTh. All these results demonstrate that the macular-scale functionality of MgH$_2$ with conductive PTh nanofilms on graphene has been successfully achieved by adopting the self-initiated polymerization. In order to verify the amount of MgH$_2$ in G/MgH$_2$@PTh, the hydrogen capacity absorbed by G/Mg@PTh for the conversion to G/MgH$_2$@PTh was detected and calculated to be 3.92 wt % (Figure S16), and no hydrogenation reaction was observed for G/PTh (Figure S16) and pure PTh under the identical condition (Figure S17). It corresponds to 51.6 wt % of MgH$_2$ NCs in G/MgH$_2$@PTh taking into account the complete hydrogenation of Mg into MgH$_2$, as reflected by the XRD results, which agrees well with the results obtained from the hydrolysis reaction (Figure S18).

The battery performance of G/MgH$_2$@PTh as electrode material was first evaluated by galvanostatic charge/discharge cycling measurements at a constant current density of 100 mA g^{-1}. The initial discharge profile consists of a plateau at ~0.9 V,

which could be attributed to the formation of solid−electrolyte interphase (SEI) films (Figure S19). A slight plateau between 0.26 and 0.04 V corresponds to the reduction of MgH$_2$ to Mg, accompanied by the formation of LiH. The XRD patterns of G/MgH$_2$@PTh (Figure 3b) elucidate the formation of LiH and Mg with the disappearance of MgH$_2$ when the electrode was discharged to 0.04 V, indicating the completion of the conversion reaction in this stage.[9] Additionally, the plateau that occurs below 0.04 V, approaching the cutoff potential, is attributed to the alloying of Mg with Li according to the XRD results, which validates the presence of hcp-type Li−Mg solid solution alloys (hcp-type Li$_x$Mg, ($x \leq 0.15$)) coupled with the absence of Mg.[9] After full lithiation, the d-spacings of the crystalline nanodomains dispersed on graphene (Figure 3c) were measured to be 0.20 and 0.28 nm, corresponding to the (200) planes of LiH and the (100) planes of hcp-type Li$_x$Mg ($x \leq 0.15$), respectively, in good agreement with the XRD results. In the first charge process, two plateaus located at 0.22 and 0.59 V are observed, corresponding to the dealloying of hcp-type Li$_x$Mg alloys and the oxidation of Mg into MgH$_2$, respectively. This could be supported by the presence of MgH$_2$ accompanied by the disappearance of LiH after charging to 3.0 V based on the *ex situ* XRD (Figure 3b) and HRTEM (Figure 3c) results. Therefore, the overall electrochemical reactions of G/MgH$_2$@PTh electrode can be described in the following equations:
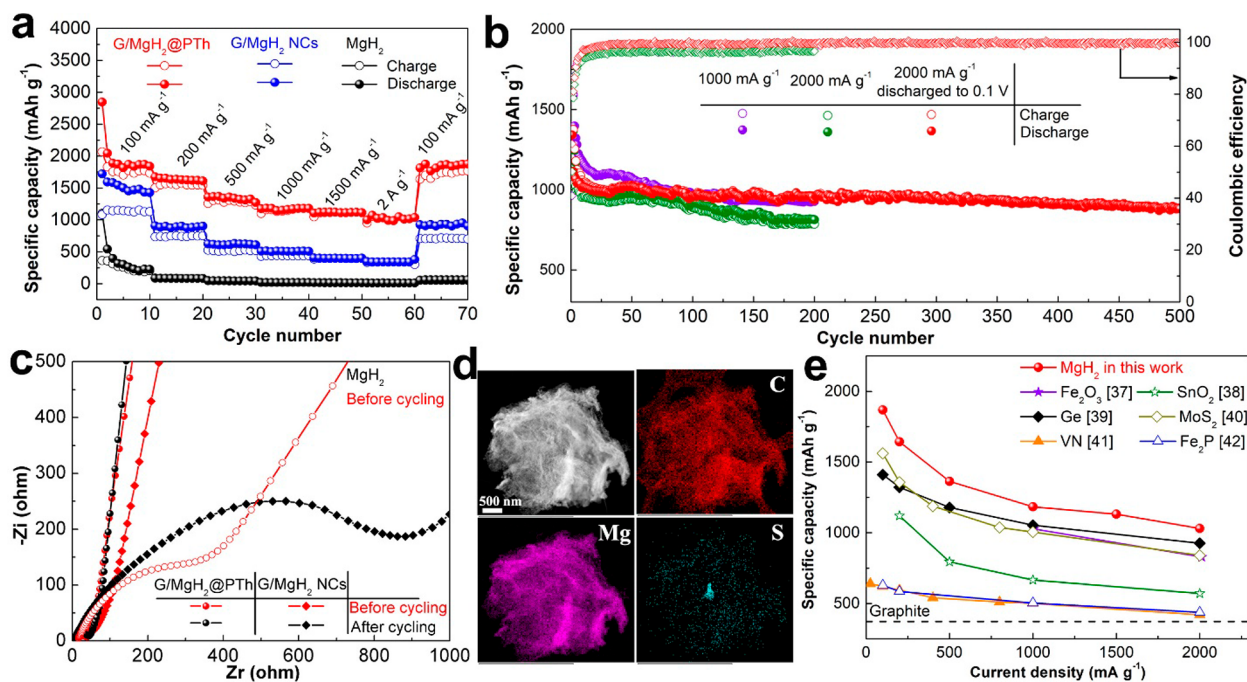
$$MgH_2 + 2Li^+ + 2e^- \leftrightarrow Mg + 2LiH \qquad (1)$$
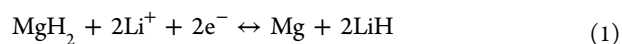
Figure 4. (a) Rate performance of G/MgH$_2$@PTh, G/MgH$_2$ NCs, and pure MgH$_2$ at various current densities. (b) Cycling performance of G/MgH$_2$@PTh and Coulombic efficiency at current densities of 1000 and 2000 mA g^{-1} in the voltage window of 0.001−3.0 V and of G/MgH$_2$@PTh at 2000 mA g^{-1} in the voltage window of 0.1−3.0 V. (c) Nyquist plots of G/MgH$_2$@PTh and G/MgH$_2$ NCs electrodes in the discharged state before cycling and after 200 cycles. (d) STEM image and the corresponding elemental mapping of G/MgH$_2$@PTh after 500 cycles. (e) Comparison of rate performance between G/MgH$_2$@PTh electrode and the recently reported values for typical metal-based anode materials, including the theoretical values of graphite for comparison. The specific capacity is calculated based on the weight of electroactive materials in the composite, assuming that the capacity contribution of other matrix in the composites is negligible.

$$17Mg + 2Li^+ + 3e^- \leftrightarrow Li_xMg(hcp), \quad (x \leq 0.15) \quad (2)$$

Remarkably, a high discharge capacity of 2846 mAh g^{-1} was achieved at a current rate of 100 mA g^{-1} for G/MgH$_2$@PTh in the first cycle (Figure 3d), which is slightly higher than the theoretical capacity of MgH$_2$ (2243 mAh g^{-1} based on the conversion reaction to form LiH and the alloying reaction to form hcp-type Li$_x$Mg alloys). It could be mainly attributed to the formation of the SEI layer on the surface and the irreversible side-reactions between the electrode and the electrolyte (Figure S19) as well as the contribution of extra capacity from the possible formation of amorphous bcc-type solid solution of Li−Mg alloys.[9] Unless otherwise noted, all specific capacities here are calculated based on the weight of MgH$_2$. In addition, the reversible capacity of the first cycle reached 1963 mAh g^{-1}, approaching the theoretical capacity of MgH$_2$. The large irreversible capacity is attributed to the formation of the SEI layer on the surface and the irreversible side-reactions between the electrode and the electrolyte. It should be noted that the performance of G/PTh was also measured under identical test conditions, as shown in Figure S20. It was confirmed that this electrode contributed negligibly to Li$^+$ storage (90 mAh g^{-1}). By comparison, the initial discharge and charge capacities of the ball-milled MgH$_2$ particles are only 1000 and 348 mAh g^{-1}, respectively (Figure 3e). Although G/MgH$_2$ NCs exhibit better electrochemical performance by taking advantage of nanocrystallization and the presence of graphene (Figure 3e), the initial discharge and charge capacities are only 1647 and 1060 mAh g^{-1}, respectively. It is interesting to note that the corresponding initial Coulombic efficiency (CE) of G/MgH$_2$@PTh reaches 68.9%, which is much higher than the corresponding values for

MgH$_2$ (34.8%) and G/MgH$_2$ NCs (64.4%). This finding indicates that the molecular-scale functionality of MgH$_2$ NCs with PTh membrane could significantly prevent the detrimental and irreversible reactions between MgH$_2$ and the electrolyte. In the second and third cycles, the CE of G/MgH$_2$@PTh dramatically increases to 88% and 91%, respectively, suggesting the rapid stabilization of the SEI layer. After 100 cycles, the reversible capacity is still as high as 1311 mAh g^{-1}, which demonstrates the high reversibility of G/MgH$_2$@PTh electrode. On the other hand, the reversible capacity of MgH$_2$ and G/MgH$_2$ NCs presents significant degradation down to only 97 and 160 mAh g^{-1}, respectively, which is ascribed to the particle aggregation and/or detachment caused by pulverization due to the large volume expansion during repeated lithiation/delithiation processes, as proved by TEM images of G/MgH$_2$ NCs after only 20 cycles (Figure S21). SEM images (Figure S22) of the electrodes after 20 cycles of discharge/charge process provide further evidence to the serious aggregation and detachment of MgH$_2$ from graphene in G/MgH$_2$ NCs, while the homogeneous distribution of MgH$_2$ on graphene is well preserved in G/MgH$_2$@PTh electrode after the same process. It further confirms that the molecular-scale functionality of MgH$_2$ with PTh could effectively alleviate the volume change upon cycling electrochemical reaction. Therefore, it is confirmed that the ultrasmall particles of MgH$_2$ NCs and graphene in G/MgH$_2$@PTh electrode enable the full utilization of MgH$_2$ NCs, leading to high reversible charge/discharge capacity, while the conformal coating of MgH$_2$ NCs with ultrathin PTh membrane controlled on a molecular level ensures the strong preservation of the nanostructure, leading to significantly improved cycling stability.

The rate capability of the anode materials is a crucial performance indicator for large-scale application of high energy and power density batteries, such as for grid-scale electricity storage and electric vehicle applications. When the current density is increased to 2000 mA g^{-1}, the reversible capacity of pure MgH_2 and G/MgH_2 NCs rapidly fades to <40 and 360 mAh g^{-1}, respectively, and only a capacity of about 767 mAh g^{-1} was regained for G/MgH_2 NCs when the current density was decreased back to 100 mA g^{-1} (Figure 4a). In marked contrast, the G/MgH_2@PTh electrode delivered a high reversible capacity of 1025 mAh g^{-1} as the current density increased to 2000 mA g^{-1}. Furthermore, the reversible capacity was restored to 1815 mAh g^{-1} when the current rate was changed back to 100 mA g^{-1}, reaching 97% of its initial discharge capacity (1868 mAh g^{-1}), demonstrating its superior reversibility. Most importantly, G/MgH_2@PTh electrode exhibited stable cycling performance over 200 charge/discharge cycles at a high current density of 1000 and 2000 mA g^{-1} (Figure 4b). After 200 discharge/charge cycles, a high specific capacity of 926 and 812 mAh g^{-1}, respectively, was obtained, corresponding to capacity retention of 79 and 80% of the 10th cycle. The continuous capacity decay is possibly attributable to the deformation of PTh membrane caused by the severe volume changes and the unfavorable reversibility of Li−Mg alloys during cycling.[9,35] Therefore, when the cutoff voltage was changed to 0.1 V to avoid the formation of Li−Mg alloys, an exceptional high discharge capacity of 884 mAh g^{-1} was achieved after 500 cycles, which equals to a capacity retention of 84.5% of the 10th cycle. The volumetric capacity is another important metric to consider for many practical applications. Taking the packing density of the G/MgH_2@PTh electrode as approximately 0.9 g cm^{-3}, the whole electrode (including graphene, PTh, and MgH_2 NCs) can deliver volumetric capacities of 422 mAh cm^{-3} at 2000 mA g^{-1} with the cutoff voltage of 0.1 V. This capacity is comparable to that of the state-of-the-art commercial graphitic anodes (i.e., 500 mAh cm^{-3}). Additionally, the CE of G/MgH_2@PTh electrode nearly reaches 100% throughout the cycling, indicating the excellent cyclability induced by the molecular-scale functionality of MgH_2 with ultrathin PTh membrane on graphene in an appropriate voltage window. The increase in the cutoff potential during the lithiation could not only reduce the volume changes, resulting in the improvement of cycle life, but also suppress the formation of lithium dendrites, resulting in enhancement of the battery safety.[36]

Electrochemical impedance spectroscopy (EIS) was further performed to understand the effects of homogeneous modification of PTh membrane toward improving the cycling performance of MgH_2 electrode (Figure 4c). The high-frequency semicircles correspond to the charge-transfer resistance, and the low-frequency oblique lines are typical Warburg behavior, ascribed to Li^+ diffusion within the electrode. The charge-transfer resistance (R_{ct}), which is a key indicator for the kinetics of the electrode, was calculated based on the fitting results (Figure S23a) according to the equivalent circuit model (Figure S23b). Apparently, G/MgH_2@PTh displays an R_{ct} of 44.4 Ω before cycling, which is lower than that of both the pure MgH_2 (221.8 Ω) and the G/MgH_2 NCs (49.3 Ω). This is mainly attributed to the synergistic effects of the highly conductive graphene and the PTh membrane and the intimate contact between them with electroactive MgH_2 NCs, which can facilitate electron transfer from the anchored MgH_2 NCs throughout the whole electrode and thus decrease

the resistance. Unfortunately, the corresponding value for G/MgH_2 NCs increased to 678.9 Ω after 200 cycles due to the formation of a thick, unstable SEI film during cycling, coinciding with large capacity decay. By contrast, the charge-transfer resistance exhibits a slight decrease for G/MgH_2@PTh to 35.7 Ω, indicating the formation of a stable SEI film and the subsequent activation process during cycling, which provides further evidence of its excellent cycling stability. Moreover, based on the relationship between Z' and $\omega^{-1/2}$ in the low-frequency region (Figure S24), where ω is the angular frequency, G/MgH_2@PTh exhibited lower slopes in comparison with G/MgH_2 NCs before cycling and after the 200th cycle, suggesting much easier Li^+ diffusion within the G/MgH_2@PTh electrode. Therefore, the significantly improved electrochemical performance of G/MgH_2@PTh in comparison with G/MgH_2 NCs could be attributed to the much higher electronic conductivity and the enhanced ionic diffusion kinetics, which were well maintained during the continuous charge/discharge cycling.

To fully understand the role of the molecular-scale functionality of MgH_2 with PTh in the cycling performance of MgH_2-based electrode, DFT calculations were further performed to examine the interaction between the electroactive species and the PTh membrane. The optimized result from the calculation (Figure S25) of the binding energy between MgH_2 and PTh was 0.46 eV, much higher than for MgH_2-graphene system (0.3 eV), which reveals the favorable molecular interaction between MgH_2 and PTh, and could enable the ultrathin PTh membrane to constrain electroactive MgH_2 NCs during cycling. Moreover, it should be noted that LiH and Mg, the discharge products of G/MgH_2@PTh electrode, also exhibit strong molecular interaction with PTh, exhibiting binding energies of 0.57 and 0.16 eV, respectively. Therefore, the theoretical calculations provide evidence for the enhancement of affinity between PTh and MgH_2, as well as the discharged products of G/MgH_2@PTh electrode, through uniform molecular interaction, which could significantly improve the structural integrity. Consequently, G/MgH_2@PTh still maintained its original appearance (Figure S20), even after the anode was charged/discharged over 500 cycles, implying the formation of stable SEI layers. Only few particles, however, could be observed in G/MgH_2 NCs after only 50 cycles. The particle size distribution exhibits that the average particle size of MgH_2 NCs is around 17.9 nm after cycling (Figure S26) with only limited increase compared to that before cycling, which corresponds well with the long cycle life of G/MgH_2@PTh and its high Coulombic efficiency. In addition, the carbon, magnesium, and sulfur element mapping (Figure 4d) verifies that the homogeneous distribution of MgH_2 NCs in G/MgH_2@PTh electrode is well preserved after cycling, which visually demonstrates the synergistic effects of both the chemical affinity and the intimate physical contact between MgH_2, as well as its discharge products, and the PTh membrane in suppressing the aggregation of electroactive NPs during repeated lithiation and delithiation. As a result, no obvious aggregation could be observed on the relatively smooth surface of the electrode with the homogeneous distribution of Mg, S, and C in the electrode (Figure S27).

It could be noted that the electrochemical properties of G/MgH_2@PTh electrode are comparable to or even much better than the state-of-art values for typical metal-based compounds, including transition-metal oxides (phosphides and/or nitrides), metal sulfides, and alloy-based metals (e.g., Ge and Sn), in

terms of specific capacity, cyclability, and rate capability (Figure 4e, Table S1).[37−42] Such superior performance can be ascribed to the following advantages: First, the self-initiated, selective, and self-limiting polymerization of thiophene monomer induced by Mg NCs, as well as the favorable molecular interaction between them, ensures the uniform and conformal coating of the MgH_2 NCs by conductive PTh nanofilms. Second, ultrasmall MgH_2 NCs significantly enhance the utilization rate of electroactive materials and tolerate the absolute strain and stress during Li^+ insertion and extraction processes. Moreover, the uniform dispersion of MgH_2 nanograins on graphene, coupled with the conformal coating of ultrathin PTh membrane, can effectively accommodate the large volume variations and inhibit particle aggregation over repeated lithiation/delithiation processes. Most importantly, the strong molecular interaction and the intimate physical contact between the ultrathin PTh membrane and the MgH_2 inside and its charge/discharge products involved in the electrochemical reactions effectively prevent detrimental reactions and promote the formation of stable SEI films, preserving the structural integrity of the electrodes over lithiation/delithiation processes during cycling and, coupled with the homogeneous distribution of graphene in the electrode, providing fast charge- and Li^+-transfer pathways. Finally, the cross-linked structure with stacked graphene enclosing MgH_2@PTh core−shell NPs inside forms a 3D conductive and mechanically robust network, so that the usage of conductive carbon and binder is avoided, which further facilitates the electron transport, Li^+ diffusion kinetics, and stable reversibility over extended cycling.

CONCLUSION

In conclusion, molecular-scale functionality of metal hydride NPs with conductive polymer on graphene has been achieved successfully *via* a self-initiated polymerization method, leading to the formation of ultrasmall MgH_2@PTh core−shell NPs uniformly distributed on graphene. The combination of ultrafine MgH_2 NCs, highly conductive graphene, and ultrathin PTh membrane synergistically improves the ion and charge transfer kinetics of MgH_2 anode. More importantly, the favorable chemical interaction and intimate contact between MgH_2 NCs, as well as the various products involved in the electrochemical reactions, and the PTh nanofilms effectively prevent detrimental reactions and improve the structural integrity during charge/discharge processes, leading to significantly improved rate performance, reversible capacity, and cycling stability. Therefore, this work presents an effective route toward developing high-capacity metal-hydride-based anodes for LIBs and pushes forward their promising practical applications. We believe that the thus-developed self-initiated polymerization route for the molecular-scale functionality of NPs and/or nanostructures may be of high interest for many other applications.

EXPERIMENTAL METHODS

Synthesis of G/MgH₂ NCs. G/MgH_2 NCs were synthesized *via* the facile hydrogenation of di-*n*-butylmagnesium ($MgBu_2$) in cyclohexane. Typically, 1.6 mL $MgBu_2$ solution (1 M in heptane) and 0.0248 g graphene were uniformly mixed in cyclohexane (40 mL) in a pressure reactor vessel. The hydrogenation reaction of $MgBu_2$ was then performed at 190 °C under 35 atm H_2 for 24 h. Finally, the solution was centrifuged and vacuum-dried at 100 °C under dynamic

vacuum on a Schlenk line, which leads to the formation of G/MgH_2 NCs.

Synthesis of G/Mg@PTh. G/Mg NCs were first fabricated *via* thermal annealing of G/MgH_2 NCs at 300 °C for complete dehydrogenation. In a typical process to synthesize G/Mg@PTh, a dry round-bottomed flask was loaded with 200 mg G/Mg NCs and 20 mL tetrahydrofuran (THF), followed by uniform dispersion using ultrasonication for 0.5 h under argon. Subsequently, 60.24 mg 2,5-dibromothiophene ($C_4H_2Br_2S$) dissolved in 10 mL THF was added dropwise, and the mixture was then heated to reflux for around 2 h to achieve uniform adsorption of thiophene monomer on Mg NCs. After further ultrasonication for 0.5 h, 0.26 mg nickel(II) 2,4-pentanedionate in 3 mL THF was supplied as the catalyst and vigorously stirred for 6 h at 65 °C. Finally, the solution was centrifuged and washed with anhydrous THF three times, and G/Mg@PTh was obtained after the removal of the solvent under dynamic vacuum for 24 h at 70 °C.

Synthesis of G/MgH₂@PTh. G/MgH_2@PTh was synthesized by the thermal treatment of G/Mg@PTh on a Sieverts apparatus under a hydrogen pressure of 100 atm at 150 °C for 10 h.

Characterizations. The crystal structure of G/MgH_2@PTh electrode was characterized by powder X-ray diffraction (XRD, D8 Advance, Bruker AXS) with Cu $K\alpha$ radiation. In order to prevent any possible chemical reactions between air and the sample during the XRD measurement, amorphous tapes were used to cover samples. Raman spectroscopy was performed on a NEXUS 670 Fourier-transform infrared (FT-IR) Raman spectrometer. The morphology of the samples was revealed by field emission scanning electron microscopy (FE-SEM, JEOL 7500FA, Tokyo, Japan) and transmission electron microscopy (TEM, JEOL 2011 F, Tokyo, Japan). Nitrogen absorption/desorption isotherms at the temperature of liquid nitrogen were obtained using a Quantachrome NOVA 4200e instrument to characterize the porous structure of the samples. The pore volumes and pore size distributions were calculated from the adsorption branches of the isotherms according to the Barrett−Joyner−Halenda (BJH) model. X-ray photoelectron spectra (XPS) was obtained on a PerkinElmer PHI 5000C ESCA system coupled with a dual X-ray source, for which an Mg $K\alpha$ (1253.6 eV) anode was adopted with a hemispherical energy analyzer. The background pressure was preserved below 10^{-6} Pa during data acquisition, and measurements were conducted at a pass energy of 93.90 eV. All binding energies were calibrated using contaminant carbon (C 1s = 284.6 eV). The hydrogen absorption properties of the as-synthesized G/Mg@PTh were investigated on a Sieverts apparatus, denoted as a gas reaction controller (GRC, Advanced Materials Corp., USA). The hydrogen absorption kinetics data were collected at 150 °C with an initial hydrogen pressure of 100 atm. The hydrolysis reaction in sulfuric acid was further performed to verify the amount of MgH_2 in the as-prepared G/MgH_2@PTh composite from the hydrogenation of G/Mg/PTh. In a typical measurement, 10 mL water was loaded into a 50 mL flask containing ~100 mg G/MgH_2@PTh composite under mechanical stirring, followed by the introduction of 4 mL H_2SO_4 (1 M) solution by 4 identical portions every minute. A desiccator composed of NaOH-CaO was used to remove the water vapor and possible acid gas from the generated hydrogen. Finally, the amount of hydrogen was quantified by water displacement in an inverted graduated cylinder over a water-filled tank.

ASSOCIATED CONTENT

Ⓢ Supporting Information

The Supporting Information is available free of charge on the ACS Publications website at DOI: 10.1021/acsnano.8b03280.

Details of electrochemical measurements and theoretical calculations, XRD, XPS, and Raman results of the as-synthesized samples (PDF)

AUTHOR INFORMATION

Corresponding Authors
*E-mail: yuxuebin@fudan.edu.cn.

*E-mail: yangzz@iccas.ac.cn.

ORCID
Zaiping Guo: 0000-0003-3464-5301
Zhenzhong Yang: 0000-0002-4810-7371
Xuebin Yu: 0000-0002-4035-0991

Author Contributions
#These authors contributed equally.

Notes
The authors declare no competing financial interest.

ACKNOWLEDGMENTS

REFERENCES

(1) Dunn, B.; Kamath, H.; Tarascon, J. M. Electrical Energy Storage for the Grid: A Battery of Choices. *Science* **2011**, *334*, 928−935.

(2) Bruce, P. G.; Scrosati, B.; Tarascon, J. M. Nanomaterials for Rechargeable Lithium Batteries. *Angew. Chem., Int. Ed.* **2008**, *47*, 2930−2946.

(3) Dudney, N. J.; Li, J. Using All Energy in a Battery. *Science* **2015**, *347*, 131.

(4) Sun, Y.; Liu, N.; Cui, Y. Promises and Challenges of Nanomaterials for Lithium-Based Rechargeable Batteries. *Nat. Energy* **2016**, *1*, 16071.

(5) Choi, N. S.; Chen, Z. H.; Freunberger, S. A.; Ji, X. L.; Sun, Y. K.; Amine, K.; Yushin, G.; Nazar, L. F.; Cho, J.; Bruce, P. G. Challenges Facing Lithium Batteries and Electrical Double-Layer Capacitors. *Angew. Chem., Int. Ed.* **2012**, *51*, 9994−10024.

(6) Tang, Y.; Zhang, Y.; Li, W.; Ma, B.; Chen, X. Rational Material Design for Ultrafast Rechargeable Lithium-Ion Batteries. *Chem. Soc. Rev.* **2015**, *44*, 5926−5940.

(7) Lee, K. T.; Cho, J. Roles of Nanosize in Lithium Reactive Nanomaterials for Lithium Ion Batteries. *Nano Today* **2011**, *6*, 28−41.

(8) Manthiram, A.; Fu, Y.; Su, Y. S. In Charge of the World: Electrochemical Energy Storage. *J. Phys. Chem. Lett.* **2013**, *4*, 1295−1297.

(9) Oumellal, Y.; Rougier, A.; Nazri, G. A.; Tarascon, J. M.; Aymard, L. Metal Hydrides for Lithium-Ion Batteries. *Nat. Mater.* **2008**, *7*, 916−921.

(10) Aymard, L.; Oumellal, Y.; Bonnet, J. P. Metal Hydrides: An Innovative and Challenging Conversion Reaction Anode for Lithium-Ion Batteries. *Beilstein J. Nanotechnol.* **2015**, *6*, 1821−1839.

(11) Huang, L.; Aymard, L.; Bonnet, J. P. MgH_2-TiH_2 Mixture as an Anode for Lithium-Ion Batteries: Synergic Enhancement of the Conversion Electrode Electrochemical Performance. *J. Mater. Chem. A* **2015**, *3*, 15091−15096.

(12) Oumellal, Y.; Zlotea, C.; Bastide, S.; Cachet-Vivier, C.; Leonel, E.; Sengmany, S.; Leroy, E.; Aymard, L.; Bonnet, J. P.; Latroche, M. Bottom-Up Preparation of MgH_2 Nanoparticles with Enhanced Cycle Life Stability During Electrochemical Conversion in Li-Ion Batteries. *Nanoscale* **2014**, *6*, 14459−14466.

(13) Zeng, L.; Kawahito, K.; Ikeda, S.; Ichikawa, T.; Miyaoka, H.; Kojima, Y. Metal Hydride-Based Materials Towards High Performance Negative Electrodes for All-Solid-State Lithium-Ion Batteries. *Chem. Commun.* **2015**, *51*, 9773−9776.

(14) Tan, G. Q.; Wu, F.; Yuan, Y. F.; Chen, R. J.; Zhao, T.; Yao, Y.; Qian, J.; Liu, J. R.; Ye, Y. S.; Shahbazian-Yassar, R.; Lu, J.; Amine, K. Freestanding Three-Dimensional Core-Shell Nanoarrays for Lithium-Ion Battery Anodes. *Nat. Commun.* **2016**, *7*, 11774.

(15) Yu, X. Y.; Yu, L.; Lou, X. W. Metal Sulfide Hollow Nanostructures for Electrochemical Energy Storage. *Adv. Energy Mater.* **2016**, *6*, 1501333.

(16) Wu, H. B.; Zhang, G.; Yu, L.; Lou, X. W. One-Dimensional Metal Oxide-Carbon Hybrid Nanostructures for Electrochemical Energy Storage. *Nanoscale Horiz.* **2016**, *1*, 27−40.

(17) Liu, N.; Lu, Z. D.; Zhao, J.; McDowell, M. T.; Lee, H. W.; Zhao, W. T.; Cui, Y. A Pomegranate-Inspired Nanoscale Design for Large-Volume-Change Lithium Battery Anodes. *Nat. Nanotechnol.* **2014**, *9*, 187−192.

(18) Zhu, Y.; Fan, X.; Suo, L.; Luo, C.; Gao, T.; Wang, C. Electrospun FeS_2@Carbon Fiber Electrode as a High Energy Density Cathode for Rechargeable Lithium Batteries. *ACS Nano* **2016**, *10*, 1529−1538.

(19) Myung, S. T.; Noh, H. J.; Yoon, S. J.; Lee, E. J.; Sun, Y. K. Progress in High-Capacity Core−Shell Cathode Materials for Rechargeable Lithium Batteries. *J. Phys. Chem. Lett.* **2014**, *5*, 671−679.

(20) Schüth, F. Encapsulation Strategies in Energy Conversion Materials. *Chem. Mater.* **2014**, *26*, 423−434.

(21) Feng, H. P.; Tang, L.; Zeng, G. M.; Tang, J.; Deng, Y. C.; Yan, M.; Liu, Y. N.; Zhou, Y. Y.; Ren, X. Y.; Chen, S. Carbon-Based Core−Shell Nanostructured Materials for Electrochemical Energy Storage. *J. Mater. Chem. A* **2018**, *6*, 7310−7337.

(22) Roy, P.; Srivastava, S. K. Nanostructured Anode Materials for Lithium Ion Batteries. *J. Mater. Chem. A* **2015**, *3*, 2454−2484.

(23) Zhang, Q. F.; Uchaker, E.; Candelaria, S. L.; Cao, G. Z. Nanomaterials for Energy Conversion and Storage. *Chem. Soc. Rev.* **2013**, *42*, 3127−3171.

(24) Zhou, W. W.; Zhu, J. X.; Cheng, C. W.; Liu, J. P.; Yang, H. P.; Cong, C. X.; Guan, C.; Jia, X. T.; Fan, H. J.; Yan, Q. Y.; Li, C. M.; Yu, T. A General Strategy toward Graphene@Metal Oxide Core−Shell Nanostructures for High-Performance Lithium Storage. *Energy Environ. Sci.* **2011**, *4*, 4954−4961.

(25) Liu, J.; Xu, X. J.; Hu, R. Z.; Yang, L. C.; Zhu, M. Uniform Hierarchical Fe_3O_4@Polypyrrole Nanocages for Superior Lithium Ion Battery Anode. *Adv. Energy Mater.* **2016**, *6*, 1600256.

(26) Mao, M.; Yan, F.; Cui, C.; Ma, J.; Zhang, M.; Wang, T.; Wang, C. S. Pipe-Wire TiO2-Sn@Carbon Nanofibers Paper Anodes for Lithium and Sodium Ion Batteries. *Nano Lett.* **2017**, *17*, 3830−3836.

(27) Zhang, B. P.; Xia, G. L.; Sun, D. L.; Fang, F.; Yu, X. B. Magnesium Hydride Nanoparticles Self-Assembled on Graphene as Anode Material for High-Performance Lithium-Ion Batteries. *ACS Nano* **2018**, *12*, 3816−3824.

(28) Wang, H.; Dai, H. Strongly Coupled Inorganic-Nano-Carbon Hybrid Materials for Energy Storage. *Chem. Soc. Rev.* **2013**, *42*, 3088−3113.

(29) Wu, S. P.; Xu, R.; Lu, M. J.; Ge, R. Y.; Iocozzia, J.; Han, C. P.; Jiang, B. B.; Lin, Z. Q. Graphene-Containing Nanomaterials for Lithium-Ion Batteries. *Adv. Energy Mater.* **2015**, *5*, 1500400.

(30) Xia, G. L.; Tan, Y. B.; Chen, X. W.; Sun, D. L.; Guo, Z. P.; Liu, H. K.; Ouyang, L. Z.; Zhu, M.; Yu, X. B. Monodisperse Magnesium Hydride Nanoparticles Uniformly Self-Assembled on Graphene. *Adv. Mater.* **2015**, *27*, 5981−5988.

(31) Yamamoto, T.; Sanechika, K.; Yamamoto, A. Preparation of Thermostable and Electric-Conducting Poly(2,5-thienylene). *J. Polym. Sci., Polym. Lett. Ed.* **1980**, *18*, 9−12.

(32) Han, M. G.; Foulger, S. H. Crystalline Colloidal Arrays Composed of Poly(3,4-ethylenedioxythiophene)-Coated Polystyrene Particles with a Stop Band in the Visible Regime. *Adv. Mater.* **2004**, *16*, 231−234.

(33) Matović, L.; Novakovic, N.; Kurko, S.; Siljegoic, M.; Matovic, B.; Popovic, Z. K.; Romcevic, N.; Ivanovic, N.; Novakovic, J. G. Structural Destabilisation of MgH_2 Obtained by Heavy Ion Irradiation. *Int. J. Hydrogen Energy* **2009**, *34*, 7275−7282.

(34) Zhang, S.; Zhu, L.; Song, H.; Chen, X.; Zhou, J. Enhanced Electrochemical Performance of MnO Nanowire/Graphene Composite During Cycling as the Anode Material for Lithium-Ion Batteries. *Nano Energy* **2014**, *10*, 172−180.

(35) Brutti, S.; Mulas, G.; Piciollo, E.; Panero, S.; Reale, P. Magnesium Hydride as a High Capacity Negative Electrode for Lithium Ion Batteries. *J. Mater. Chem.* **2012**, *22*, 14531−14537.

(36) Lin, L.; Xu, X.; Chu, C.; Majeed, M. K.; Yang, J. Mesoporous Amorphous Silicon: A Simple Synthesis of a High-Rate and Long-Life Anode Material for Lithium-Ion Batteries. *Angew. Chem., Int. Ed.* **2016**, *55*, 14063−14066.

(37) Cao, K. Z.; Jiao, L. F.; Liu, H. Q.; Liu, Y. C.; Wang, Y. J.; Guo, Z. P.; Yuan, H. T. 3D Hierarchical Porous α-Fe_2O_3 Nanosheets for High-Performance Lithium-Ion Batteries. *Adv. Energy Mater.* **2015**, *5*, 1401421.

(38) Zhou, X.; Yu, L.; Lou, X. W. Formation of Uniform N-Doped Carbon-Coated SnO_2 Submicroboxes with Enhanced Lithium Storage Properties. *Adv. Energy Mater.* **2016**, *6*, 1600451.

(39) Zhang, W.; Chu, X. Q.; Chen, C. J.; Xiang, J. W.; Liu, X. X.; Huang, Y. H.; Hu, X. L. Rational Synthesis of Carbon-Coated Hollow Ge Nanocrystals with Enhanced Lithium-Storage Properties. *Nanoscale* **2016**, *8*, 12215−12220.

(40) Yu, S. H.; Lee, D. J.; Park, M.; Kwon, S. G.; Lee, H. S.; Jin, A. H.; Lee, K. S.; Lee, J. E.; Oh, M. H.; Kang, K.; Sung, Y. E.; Hyeon, T. Hybrid Cellular Nanosheets for High-Performance Lithium-Ion Battery Anodes. *J. Am. Chem. Soc.* **2015**, *137*, 11954−11961.

(41) Zhao, D.; Cui, Z.; Wang, S.; Qin, J.; Cao, M. VN Hollow Spheres Assembled from Porous Nanosheets for High-Performance Lithium Storage and the Oxygen Reduction Reaction. *J. Mater. Chem. A* **2016**, *4*, 7914−7923.

(42) Zhang, Y.; Zhang, H.; Feng, Y.; Liu, L.; Wang, Y. Unique Fe_2P Nanoparticles Enveloped in Sandwichlike Graphited Carbon Sheets as Excellent Hydrogen Evolution Reaction Catalyst and Lithium-Ion Battery Anode. *ACS Appl. Mater. Interfaces* **2015**, *7*, 26684−26690.